2023

CAPTURING MICROSTRUCTURAL HETEROGENEITY AND PREDICTING LOCAL TRANSPORT PHENOMENA IN PEMFC CATALYST LAYERS: A COMPREHENSIVE NETWORK MODELING APPROACH

Shahriar Alam
Michigan Technological University, salam2@mtu.edu

CAPTURING MICROSTRUCTURAL HETEROGENEITY AND PREDICTING LOCAL TRANSPORT PHENOMENA IN PEMFC CATALYST LAYERS: A COMPREHENSIVE NETWORK MODELING APPROACH

By

Shahriar Alam

A THESIS

Submitted in partial fulfillment of the requirements for the degree of

MASTER OF SCIENCE

In Mechanical Engineering

MICHIGAN TECHNOLOGICAL UNIVERSITY

2023

This thesis has been approved in partial fulfillment of the requirements for the Degree of MASTER OF SCIENCE in Mechanical Engineering.

Department of Mechanical Engineering-Engineering Mechanics

Thesis Advisor: *Dr. Jeffrey S. Allen*

Committee Member: *Dr. Kazuya Tajiri*

Committee Member: *Dr. Youngchul Ra*

Committee Member: *Dr. Rajesh Ahluwalia*

Department Chair: *Dr. Jason R. Blough*

Dedication

To my parents, fellow brothers and sisters

This work is dedicated to the unwavering love and sacrifices of my parents. Throughout my life, they have dedicated themselves to my happiness, often at the cost of their own. Miles may separate us, but their unwavering support and encouragement have been my guiding light. I dream of a day when, by the grace of the Almighty, we will be reunited.

In the interim, I commit myself to working diligently to create a future where our paths converge. To my parents, your sacrifices are the foundation upon which this work stands, and I dedicate its success to you.

Additionally, this work is dedicated to all my brothers and sisters across the globe who endure injustice. May the Almighty grant me the means to utilize my knowledge to contribute towards a world where justice and equality prevail. Let this work be a small step towards a future where suffering is alleviated, and hope is restored.

Contents

List of Figures

List of Tables

Preface

Fuel cells, specifically Proton Exchange Membrane Fuel Cells (PEMFCs), stand as beacons of promise in the realm of clean energy solutions. These remarkable devices hold the potential to revolutionize our approach to power generation, offering an environmentally friendly alternative that aligns with our collective commitment to a sustainable future. Yet, unlocking their full potential requires a nuanced understanding of the microstructural intricacies within PEMFC catalyst layers and the profound impact of local transport phenomena.

In the pursuit of unraveling these complexities, this master's thesis, titled Capturing Microstructural Heterogeneity Predicting Local Transport Phenomena in PEMFC Catalyst Layers: A Comprehensive Network Modeling Approach, introduces a groundbreaking network architecture. At its core, this unique approach encompasses separate networks comprising countless cylindrical elements and nodes, meticulously representing the solid and pore phases of the catalyst layer. Transport resistances are intricately assigned to the elements, while the nodes, though volumeless, serve as repositories for vital local properties.

The interlinking of these networks through nodes becomes the crucible where local properties are stored, forming the foundation for the proposed computational grid.

The macroscopic behaviors of this grid, including percolation behavior, gas diffusivity, and ion conductivity, are meticulously calibrated against experimental data, validating the precision of the proposed model.

This research extends beyond the confines of theoretical abstraction; diffusion-like transport equations are artfully applied to the networks, offering insights into the local water balance, active reaction sites, temperature distribution, and concentration of species within the catalyst layer across diverse fuel cell operating scenarios. The implications of this work are far-reaching; the proposed modeling approach not only enhances our fundamental understanding of PEMFC behavior but also emerges as a practical manufacturing guideline and testing tool for fuel cell catalyst layers.

In the course of this academic odyssey, I have been profoundly fortunate to be guided by a cadre of brilliant minds and supportive mentors. Their wisdom, encouragement, and unwavering belief in the significance of this research have been instrumental in shaping the trajectory of this thesis. To my advisors and the members of my research committee, I extend my heartfelt gratitude for their invaluable insights and constructive critiques.

I also express my deep appreciation to my colleagues and peers whose stimulating discussions and shared enthusiasm have enriched this research journey. Additionally, I am indebted to my family and friends, whose boundless encouragement and understanding have sustained me through the challenges of this endeavor.

As this thesis finds its place in the academic discourse, I am filled with a sense of fulfillment and anticipation. It is my fervent hope that this work will not only contribute meaningfully to the field of fuel cell technology but also inspire future generations of researchers and innovators to explore the uncharted realms of scientific inquiry.

Acknowledgments

I extend my heartfelt gratitude to the Mechanical Engineering and Engineering Mechanics Department at Michigan Tech for their generous financial aid, which has significantly supported my pursuit of a Ph.D. This invaluable assistance has enabled me to focus on my research and academic endeavors. I am also deeply thankful to the Department of Energy (DOE) for sponsoring my attendance at various conferences, enriching my academic experience and fostering connections within the scientific community. Special appreciation goes to Dr. Iryna Zenyuk, Dr. Andrew Haug, and Dr. Kazuya Tajiri for their insightful advice and guidance throughout the course of my work. Dr. Ezequiel Medici deserves special mention as the visionary behind the network modeling approach for PEMFC CL, contributing significantly to the advancement of my research. I would like to express my gratitude to my advisory committee for their valuable input and support. I am eager to learn from each member and strive to excel under their guidance. A sincere thank you to the members of my research group, MnIT, for their unwavering support, guidance, and inspiration. Your collective contributions have been instrumental in the progress of my research. My deepest appreciation goes to my supervisor, Dr. Allen. Serving as your Ph.D. student has been an honor, and I am grateful for your patience, mentorship, and guidance. Your support has been pivotal to my academic journey, and I am thankful for it now and always. Lastly, I offer my utmost gratitude to the Almighty for everything that

I am and I have. Alhamdulillah.

Nomenclature

Pt	Platinum
I/C	Ionomer to carbon ratio
k^s	Thermal conductivity
Δh^e	Phase change enthalpy
$(\rho c_p)^s$	Solid heat capacity
$(\rho c_p)^l$	Liquid heat capacity
ϵ_o	Absolute permittivity
ϵ_r	Relative permittivity
R_g	Universal gas constant
R_o	Reference channel radius
F	Faraday constant
G	Shear modulus
P^g	Gas pressure
T	PEMFC operating temperature
RH	Relative humidity
γ	Surface tension of water
α	Reorganization factor
ρ_p	Density of dry polymer

IEC	Ion exchange capacity
θ	Contact angle
V_w	Molar volume of water
k_B	Boltzmann constant
C_g	Gas concentration
q_e	Electron charge
c_o	Proton concentration
R_{ij}	Ionomer network element radius
l	Network element length
m^{ev}	mass of evaporating liquid water
c_p	Specific gas constant
r_s	Carbon network element radius
r_p	Pore network element radius
S_{ij}	Fraction of liquid water in a pore element
D^w	Water diffusivity in ionomer
$D^{g,a}$	Gas (vapor or oxygen) diffusivity in air
x_{ij}	Liquid water meniscus position in a pore network element
μ_{eff}	Effective viscosity of liquid water
p	Liquid water pressure
p^c	Capillary pressure
ϕ	Radial swelling parameter

η	Ionomer network element swelling parameter
G	Modulus of elasticity of ionomer
η_c	Critical swelling parameter
P^l	Liquid pressure in ionomer network
σ_o	Surface charge density of ionomer network element
$\bar{\sigma_o}$	Mean surface charge density
R_c	Critical channel radius
ρ_{SO_3}	Sulphonic acid group density
λ_{ij}	Water uptake by ionomer network element
λ	Overall Water uptake in the catalyst layer
$N^-_{SO_3}$	total number of sulphonic acid group in an ionomer network element
$\frac{\Delta V}{V_o}$	Volumetric change in ionomer due to water absorption

Abstract

A unique network architecture that captures the microstructural heterogeneity and predicts the local transport properties of PEMFC catalyst layers is proposed. Separate networks containing numerous cylindrical elements and nodes are generated that represent the solid and pore phase of the catalyst layer. Transport resistances are assigned to the elements while the nodes are volumeless. The networks are interlinked through nodes where local properties are stored. The generated computational grid's macroscopic behaviors (percolation behavior, gas diffusivity, and ion conductivity) will be matched against the experimental data for validation. Diffusion-like transport equations are applied to the networks that provide local water balance, active reaction sites, temperature distribution, and concentration of the species in the catalyst layer at various fuel cell operating scenarios. The proposed modeling approach can be used as a manufacturing guideline and testing tool for fuel cell catalyst layers.

Chapter 1

Introduction

Proton Exchange membrane fuel cell (PEMFC) is a power-generating electrochemical device that has anode and cathode separated by a polymer electrolyte membrane. Hydrogen oxidizes into protons and electrons in the anode. Protons travel through the electrolyte to reach the cathode side, where it reduces to H_2O by reacting with O_2. The electrochemical reaction is represented as:

$$4H^+ + 4e^- + O_2 \rightleftharpoons 2H_2O + \text{Heat} \tag{1.1}$$

Electrons reach the cathode side through an external circuit. Power, heat, and water are generated in the porous cathode catalyst layer. The solid components of these layers are ionomer or polymer electrolyte material and carbon support. The carbon

serves as a conductor for both electrons and thermal energy. The carbon portion of the catalyst layers has randomly dispersed catalyst particles (Platinum). The ionomer serves primarily as a proton transporter to the reaction sites and can also hold water. The pores of catalyst layers play a crucial role in oxygen reaching these reaction sites or embedded Pt catalyst particles. And inside this very thin layer, all the primary transfer mechanisms and energy generation occur. It is, therefore, one of the most critical components for proper PEMFC performance.

The quantity of water formed within the catalyst layer is intricately connected to its microstructural properties, local transfer phenomena, active surface area, and fuel cell operating conditions. Too much water floods the fuel cell porous media, making it difficult for oxygen to reach the catalysts. Insufficient water hinders proton delivery to the reaction sites, reduces overall efficiency. Therefore, proper hydration is essential for maximum energy output. Thus, it is crucial for effective fuel cell operation to have a firm grasp on the interplay between local morphology, transport phenomena, reaction kinetics in catalyst layers, and the overall operating environment.

Since obtaining local transport characteristics and their interlink with the macroscopic properties and overall fuel cell performance is extremely difficult, models of all the transport phenomena mentioned above combined with simulation and diagnostic tools can be advantageous in order to gain a deeper understanding of this facet. Here,

a novel network architecture is proposed. The intent is to capture the microstructural properties of PEMFC catalyst layers and predict the interplay between all the local transport phenomena (water and reactant movement in the void space, proton transport, and water retention in the ionomer, heat transport in the carbon).

1.1 Background

1.1.1 Network modeling approach

The network model, commonly called the pore-network model, is a valuable analytical tool for investigating the characteristics of porous media. The technique mentioned above is extensively employed within the field of petroleum engineering to examine the movement of fluids in reservoirs containing oil and gas. It is also used in soil science to explore the processes of water and nutrient absorption by plants. In network models, the void space of porous media is typically depicted as a two- or three-dimensional network of nodes connected by cylindrical elements. The vacuum space of a porous medium can be distributed across either the pore nodes or the connecting cylindrical elements. Ioannidis [1] and Chang [2] have assigned the pore volume to the nodes, while the elements function solely as conductors. Aker and Al-Gharbi [3, 4] employs a methodology in which the void volume and conductance are assigned

to the network elements while the nodes are devoid of volume. Rooaf [5] utilizes a network technique that accounts for the transport volume in both pore nodes and elements. Linear transport equations, as elaborated in section 3.1.1, are employed to the pore network elements and the nodes to derive the overall properties (porosity, permeability, diffusivity, fluid saturation, etc.) and local transport characteristics of a porous media.

1.1.2 Network model approaches in PEMFC modeling

Network models have been popular in the fuel cell field because they efficiently capture local phenomena in multiphase systems and have a wide range of applicability. These methods have been extensively utilized to track local water and gas inside Porous Transport Layer (PTL) or Gas Diffusion Layer (GDL). The porosimetry test and gas permeability data of two distinct gas diffusion layers (GDL) were used by Gostick [6] to calibrate the pore network incorporating pore nodes and elements. Drainage conditions that estimate how water and gases are distributed locally inside the GDL were demonstrated. Additionally, the model was utilized to investigate the current generation limiting conditions at varying degrees of water saturation in the GDL. Sinha [7] used a similar method to examine flooding within GDL for various GDL morphology. All the pore volume is assumed to be confined by pores in the techniques above. Medici employs a distinct approach in which nodes are devoid of volume, while

the cylindrical elements of the network are assigned transport volume and resistances [8]. Using structured elements and nodes, they effectively captured the unstructured morphology of gas diffusion layers (GDLs). Their investigation focused on examining liquid water saturation within the pore network. The study analyzed the impact of variations in contact angles and morphological changes on local water distributions. The findings revealed that local morphological randomness had a more substantial influence on the local water distribution than contact angle variation (a macroscopic property). The impact of evaporation on the local distribution of water and overall saturation within the gas diffusion layer (GDL) was also examined by Medici [9].

1.1.3 Network model approaches in analyzing catalyst layers

Despite their enormous potential, fuel cell electrodes have rarely been modeled using network techniques. Within the cathode electrode, multiple pathways transfer protons, electrons, O_2, and water (in both its liquid and vapor phases). The electrochemical current generated at the cathode catalyst layers results from a complex interplay between all these transport processes. In addition, it is challenging to capture the catalyst layer local morphology using network architecture since catalyst layer microstructural properties are entirely different from those of GDLs or any porous media. Several attempts have been made to simulate the movement of liquid water within the pores of cathode electrodes by El Hannach and coworkers[10, 11]. A

cathode catalyst layer was recreated as a two-network system - one network consisting of interconnected aggregates in which heat, electron, and proton transport equations were implemented. Gas diffusion and liquid water percolation were considered in the pore network between the electrode aggregates. The aggregates contain ionomer, carbon, and catalyst particles. They effectively correlated the electrochemical reaction with the consumption of the reactant and charge transport. Only the agglomerates producing liquid water were regarded as active, and the number of active agglomerates and the production of liquid water were model inputs. The model provides relevant information regarding the percolation of liquid water through sub-micron pores, the time of breakthrough, and the quantity of current created based on the number of active agglomerates. The models also provide species local concentrations at various fuel cell operating environments.

1.2 Objectives and Goals

The goal is to build a computationally efficient simulation tool for a fuel cell cathode catalyst layers and use this tool to understand the interlink between the microscopic heterogeneity of catalyst layers and PEMFC operational performance. The model proposed here can be a cost-effective premanufacturing guideline and post-manufacturing testing tool for PEMFC catalyst layers.

1.2.1 Capturing microstructural heterogeneity of catalyst layers

Macroscopic parameters of a catalyst layer include the ratio of ionomer to carbon (I/C), the volumetric percentage of ionomer, the Pt loading, the Pt/C ratio, the porosity, and the electrochemically active surface area. By constructing structured linked network systems from macroscopic features, the described method can capture the microstructural complexity inside a catalyst layer. The procedure is straightforward, economical, and computationally efficient.

1.2.2 Influence of local transport processes on overall PEMFC performance

This novel architecture will provide a clear understanding of the interplay between local transport processes and an idea of what occurs within a catalyst layer during PEMFC operation. The local transport processes include water and O_2 movement in the void space, proton movement and water uptake by the ionomer, and heat transport through carbon. The electrochemical reaction will be simulated in the catalyst sites to generate power. Ex-situ analysis of these electrochemical and transport phenomena is improbable, and in-situ analysis is highly challenging, even with the most advanced

imaging technologies.

1.2.3 Effect of local morphology on bulk transport properties of catalyst layers

Bulk transport qualities are essential for the efficient transport of reactants to the electrocatalysts, water drainage from the catalyst layer, and heat management, i.e., optimal PEMFC performance. The given method will be capable of determining the bulk transport properties of the catalyst layers and the effect of local morphological variation on those qualities.

Chapter 2

Network Generation Algorithm

2.1 Element size distribution and catalyst layer realization

Three unique network architectures are produced for the catalyst layer ionomer, carbon, and void space. Each network is comprised of several cylindrical elements, all of which are connected by nodes. Transport volume and resistance are assigned to elements while nodes are considered volumeless. The local potentials are saved at the nodes. Element lengths are fixed but have varying resistance that is related to element cross-section. This variation will ensure a random distribution of transport

resistances throughout each network. The Figure 2.1 summarises the transport resistance distribution and network generation process. Each node in the solid-phase network architecture is accompanied by a random number of catalyst particles that function as sources and sinks for the overall network. The schematic diagram of the network architecture for the catalyst layer is provided in Figure 2.2.

2.1.1 Determining the element length

The mean pore size (radius) is obtained from an actual catalyst layer. If the generated computational domain is 3D, inputs are L (length), H (thickness), and W (width). On the other hand, if the domain is 2D, the model inputs are L and H. The domain size, dimensions, and mean pore size undergo an iterative process to give an appropriate element length for the computational domain. This element length is constant throughout all the elements of the networks. The iterative process is documented by Konduru [12]

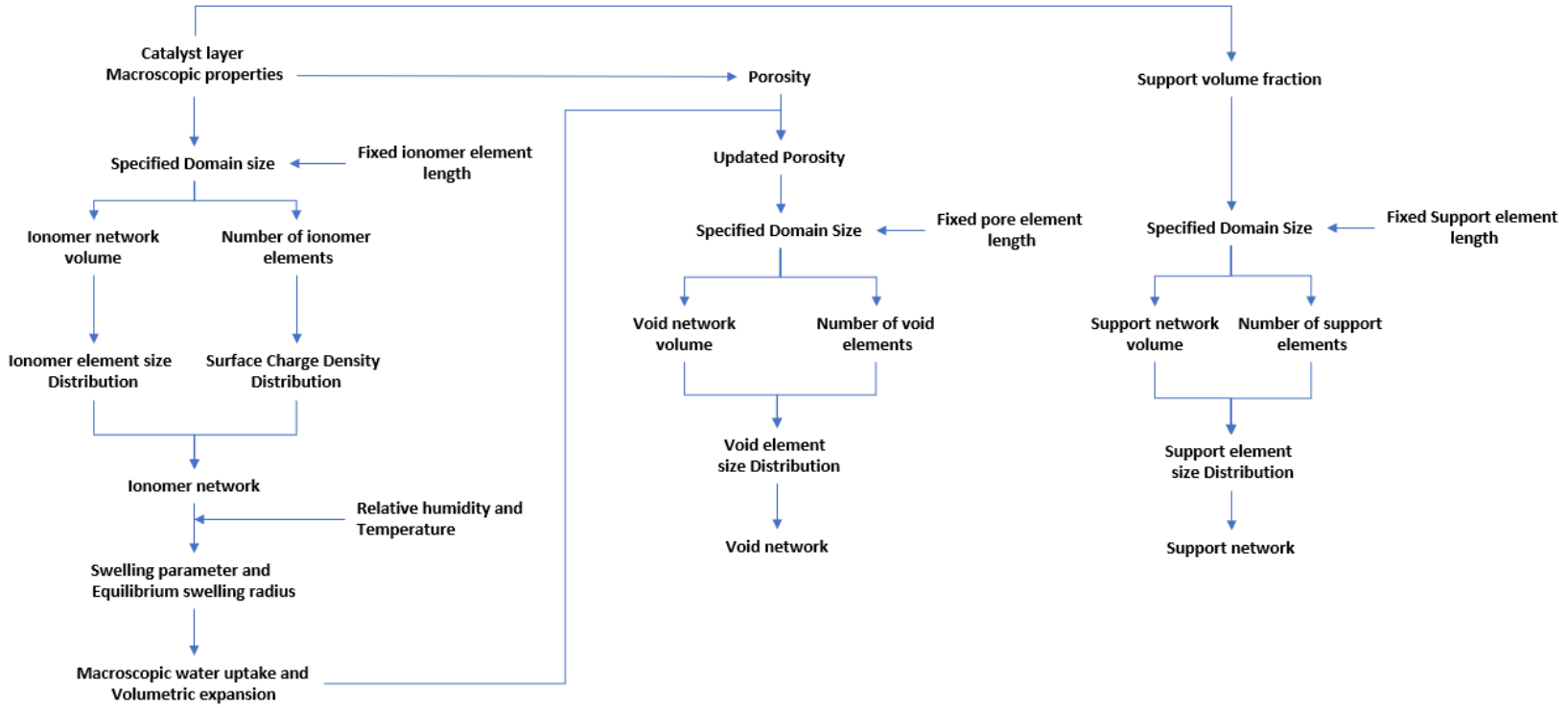

Figure 2.1: Network Generation Algorithm

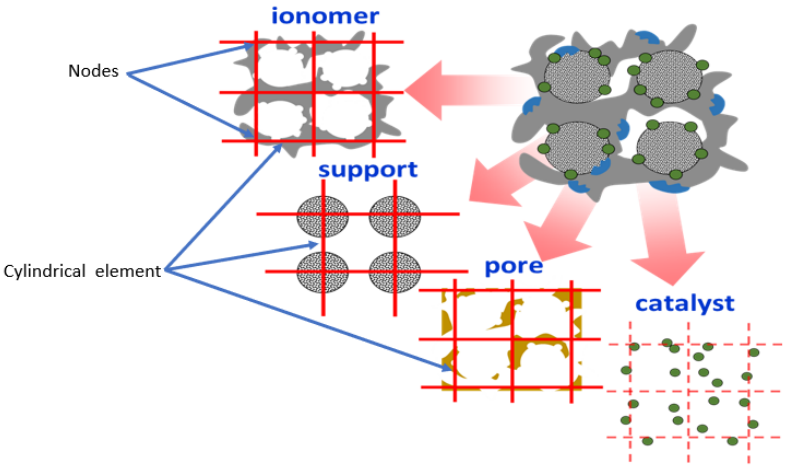

Figure 2.2: Schematic diagram of proposed network architecture for catalyst layer

Table 2.1
Inputs for Catalyst Layer grid generation

Properties	Value	Units
Bulk porosity	50%	
Volume fraction of Pt	0.028	
Pt loading per unit area	2.5	gm^{-2}
Volume fraction of ionomer	0.11	
Electrochemical Active Surface Area	100	m^2g^{-1}
Ionomer to carbon ratio	1	
Whisker length	0.1	μm
Whisker diameter	0.1	μm
Pt to carbon ratio	1	
Whisker ionomer coverage	50%	
Computational domain length	500	μm
Computational domain thickness	3	μm
Carbon element length	0.4	μm
ionomer element length	0.4	μm
Pore element length	0.4	μm
Whisker spacing	0.04	μm

2.1.2 Carbon network

An actual catalyst layer is analyzed to determine the carbon loading and the ionomer to carbon (I/C) ratio. We can calculate the network's carbon volume with these macroscopic characteristics and the designated domain size. The number of carbon elements is determined by the fixed length of the carbon elements and the domain dimension. Then, a size or radius distribution for the carbon elements is developed so that the total number of elements and the total volume contained by carbon in the network remains constant. These sizes are randomly applied to the elements to generate the carbon network.

2.1.3 Pore-phase network

The domain size and porosity of the actual catalyst layer provide us with the pore volume of the generated computational domain. The dimension of the computational domain and the number of elements decide the number of pore elements to populate the grid. A pore size distribution or pore radii distribution is generated by conserving the number of pore elements and the void volume. The generated radii are then randomly assigned to the pore elements to create a pore network containing elements of fixed length but varying radii. When injected, fluid forms menisci and percolates

from one pore element to another, finding the least resistive path and increasing percolation pressure until it exits the domain.

2.1.4 Ionomer network

The volumetric fraction of the ionomer, the Ionomer to carbon (I/C) ratio, porosity, and the size of the generated catalyst layer computational domain provide the total ionomer volume. The specified domain size and predetermined element length determine how many ionomer network elements are required to fill the whole domain. The average radius is found by keeping the number of ionomer network elements and the volume of the ionomer the same. To introduce heterogeneity, surface charge densities are randomly assigned to the ionomer network elements from a surface charge density distribution, while each element contains the calculated average radius. When exposed to different relative humidities (RH), these elements swell and open up channels inside to hold water and transport proton. The equilibrium swollen channel radius can be obtained from a swelling parameter that is a function of the surface charge density, external liquid pressure, temperature, and ionomer material properties. So, even if all the elements have the same local temperature, hydration, material properties, and thickness, the surface charge density can cause them to hold different amounts of water and have different water channel radii inside.

2.1.5 Catalyst layer realization

Combining three networks with catalyst particles is a realization. The catalyst layer realizations have the same macroscopic properties and element size distributions, but the random dispersion of each network's element sizes, as described above, is mutually exclusive from one realization to another. Hence, the only difference across realizations is the orientation of each network's transport resistances. The macroscopic properties of the catalyst layer and the fixed element lengths used to generate the network architecture are provided in the Table 2.1:

Chapter 3

Transport Equations

3.1 Decription of governing equation

One-dimensional transport equations are applied to each elements, while local potentials are maintained at the nodes. The local potentials are O_2, H^+ concentration, relative humidity, temperature, liquid water pressure, and λ (water uptake). The active sites mimic the platinum particles that are dispersed throughout the catalyst layer. These sites are not interconnected but they work as the source and sink to the ionomer, carbon, and pore network nodes. Water uptake in the ionomer elements is modeled and includes swelling. Water transport in the pore-network elements is modeled as Hagen-Poiseulle flow with the addition of capillary pressure. Water vapor

and O_2 transport in the pore-network element is modeled as diffusion. For heat transport, the conduction equation is applied to the carbon network elements, providing the local temperature distribution. Evaporation of water is also taken into account. In order to simulate the Oxygen Reduction Reaction (ORR), a modified double-trap kinetic model is applied at the catalyst sites.

3.1.1 Basic transport model

All the transport equations in this context are, essentially, diffusion equations. Speices' flux depends upon a potential difference across the element and spatially varying transport resistance. The potentials are the local properties stored at the nodes. The resistances are assigned to the elements and vary based on the sizes randomly assigned to the elements based on the element size distribution curve. To capture the microscopic characteristics, we are, in principle, dispersing resistance throughout the networks.

3.1.2 Heat transport in carbon network

To track the temperature and take into consideration evaporation in the liquid water in the pore phase, the energy conservation equation is used at each carbon node as

explained by Surasani Surasani2008a:

$$m_i c_p \left(\frac{dT_i}{dt}\right) = \dot{Q}_{ij} - \sum_{j=1}^{n_p} (\dot{m}^{\mathrm{ev}} \Delta h^e)_{ij} \tag{3.1}$$

The first term of the right-hand side of the equation is the source term which signifies the heat generated at the catalyst sites due to the oxygen reduction reaction. Heat is transported through a carbon network element and updates the nodal temperatures as:

$$Q_{ij} = \frac{k^s A}{l} (T_i - T_j) \tag{3.2}$$

The solid thermal conductivity of an element is k^s. The area of the carbon network element is A and the length of the element is l_s. The energy needed to evaporate liquid water with a mass of $\dot{m}^{\mathrm{ev}}$ is represented by the second term in Equation 3.1. This term will be zero if no liquid water is in the pore elements surrounding that carbon node. The communicative variable between the carbon and the pore network is water. The phase change enthalpy is Δh^e. The calculation of evaporating liquid mass will be covered in detail later. n_p represents the number of pore network components connected at that node, and n_w refers to the number of catalyst particles that are present surrounding the carbon node i. Large amounts of water production and small pore sizes can lead to condensation and the flooding of catalyst layers' pore space. As part of the model development described in 5.1.4, our proposed research will investigate condensation as a function of water vapor pressure and local temperature.

The total heat capacity of the cylindrical channels surrounding any carbon node is indicated here by the expression $m_i c_p$, which varies from node to node depending on the geometry of the connected pore and carbon network elements. The total heat capacity at each node depends on both the heat capacity of carbon and the amount of water in the cylindrical pore channels around node i. It's calculated by multiplying carbon and liquid heat capacities with the corresponding occupied volume. The total heat capacity of node i is:

$$m_i c_p = \frac{l_s}{2} \sum_{j=1}^{n} \left(\pi r_{s,ij}^2 (\rho c_p)^s + S_{ij} \pi r_{p.ij}^2 (\rho c_p)^l \right) \tag{3.3}$$

Here, $(\rho c_p)^s$ and $(\rho c_p)^l$ are the solid and liquid heat capacities respectively. $r_{s,ij}$ and $r_{p,ij}$ are respectively the connected carbon element and pore element radius at that node and S_{ij} signifies the fraction of liquid water-air present in the pore element.

3.1.3 Water and gas transport in pore network

Liquid water movement inside a cylindrical pore network element follows pressure-driven flow [3]. Water will displace the already-filled O_2. Transport of water between two adjacent nodes is described as:

$$q_{ij} = \kappa \frac{r_{p.ij}^4}{\mu_{ij}^{\text{eff}} l} \left(p_i - p_j - p_{ij}^c \right) \tag{3.4}$$

here q_{ij} is the local flow rate of liquid water from pore network node i to j. p_i and p_j are the nodal liquid pressures. p_{ij}^c is the local capillary pressure due to the interaction between liquid water and O_2 in the cylindrical channel. κ is the proportionality constant which is taken as $\pi/8$ and accounts for the permeability of the porous media. μ_{ij}^{eff} is the effective viscosity that depends on the interaction between liquid water and O_2 inside the pore network element and it's dependent on the liquid water position inside the element. The effective viscosity and the capillary pressure p_{ij}^c as a function of advancing liquid meniscus is calculated in the same manner as [9]. Conservation of mass is applied at each node to obtain a linear system of equations in terms of the unknown local pressures at each pore network node.

Water vapor and O_2 move through the pore network elements due to a concentration gradient. Their flow rates q_g are expressed as:

$$q_g = \frac{\pi r_{p,ij}^2 D^{g,a}}{l} \left(C_{g,i} - C_{g,j}\right) \tag{3.5}$$

where g can be O_2 or water vapor. $D^{g,a}$ means the diffusivity of the species in air, while the nodal concentrations expressed by C_g. Diffusion of O_2 through a liquid water-filled pore network element is ignored as its diffusivity in water is sluggish compared to in the air [13].

3.1.4 Evaporation and Updating Liquid Water Menisci

Fuel cell evaporation is governed by a diffusion-limited model that requires a change in partial pressure to initiate a phase transition [14]. Evaporation updates the liquid water menisci position inside a pore network element. Through equation 3.1, this also revises the carbon network's temperature distribution. The evaporating liquid mass is calculated as:

$$m_{ij}^{\mathrm{ev}} = \frac{\pi r_{p,ij}^2 \Delta t D_{ij}}{l} \left(C_i^{\max} - C_j\right) \tag{3.6}$$

The simulation timestep is Δt, and D_{ij} represents local temperature-dependent vapor diffusivity. C_j is the vapor concentration at local relative humidity and $C^{\max}i$ is the saturated vapor concentration at local temperature. The menisci position inside a pore element is calculated as:

$$x_{ij} = \frac{m_{ij}^l - m_{ij}^e}{\pi r_{p,ij}^2 \rho^l} \tag{3.7}$$

ρ^l and m_{ij}^l represent the liquid water density and liquid mass within the pore element, respectively. Only when x_{ij} is positive will we observe the menisci of liquid water within the pore element. A value of zero indicates that the menisci are in the same position as in the preceding time step. If x_{ij} is negative, the pore element has totally dried out and there are no liquid water menisci therein. If x_{ij} exceeds the length of the pore element, the excess volume of moving menisci is injected into the pore elements attached to the pore node at the other end of the current source node.

3.1.5 Water and proton transport in ionomer network

The simulation of ionomer network swelling and water absorption has been conducted utilizing the principles of poroelastic theory. The phenomenon is elucidated in [15] where the authors derive an equation of state for water within a single ionomer pore element by employing a comprehensive approach that considers the thermodynamic equilibrium conditions associated with capillary, osmotic, and elastic phenomena. Applying surface charge density at the pore wall they obtain a swelling parameter and equilibrium swollen state of a single membrane pore. Here, we randomly distribute surface charge densities across the elements of the ionomer network and apply the swelling model in the literature to each of the elements. Under specific temperature (T) and humidity (RH) conditions, the swelling model provides swelling parameters against various applied surface charges to the ionomer elements. The swelling degree and radius of the swollen water channel inside an ionomer element are calculated from the swelling parameter. The process is described below:

$$\sigma_{o,ij} = \frac{2\epsilon_o\epsilon_r R_g T}{FR_o}\left(\frac{\phi}{\eta_{ij}}\right)^{\frac{1-\alpha}{1+\alpha}}\left\{1-\left[1+\left(\frac{FR_o^2}{2\epsilon_o\epsilon_r R_g T}\right)\left[\frac{2}{3}G\left(\left(\frac{1}{\eta_{ij}+1}\right)^{1/3}-\left(\frac{1}{\eta_{ij}+1}\right)^{7/3}\right)-P^l\right]\left(\frac{\phi}{\eta_{ij}}\right)^{\frac{-2}{1+\alpha}}\right]\right\}^{1/2} \quad (3.8)$$

$\sigma_{o,ij}$ is the surface charge density assigned to an ionomer element, ϵ_o is the absolute permittivity, and ϵ_r is the temperature-dependent relative permittivity of water. Rg represents the universal gas constant, and T is the temperature at which the ionomer element is exposed. F is the Faraday constant, while Ro is a constant reference channel radius. G represents the shear modulus of ionomer. η is the swelling parameter, P^l is the liquid pressure incorporating relative humidity, and α is the reorganization factor. P^l is expressed as:

$$P^l = P^g - \left(\frac{2\gamma}{R_o}\right)\left(\frac{\phi}{\eta_c}\right)^{1/(1+\alpha)} \tag{3.9}$$

Here, P^g is the gas pressure, γ is the temperature-dependent surface tension of water, and η_c is the critical swelling parameter. ϕ, is called the radial swelling parameter, which is constant for PEM material properties and surface charge density distributions. It is written as:

$$\phi = -\frac{R_o \rho_{SO_3^-}}{2\bar{\sigma_o}} \tag{3.10}$$

$\bar{\sigma}_o$ is the mean surface charge density from the surface charge density distribution. The sulfonic acid group density, ρ_{SO_3} is calculated as:

$$\rho_{SO_3} = \text{IEC}\, F\, \rho_p \tag{3.11}$$

Here IEC is the ion exchange capacity and ρ_p is the density of dry polymer. The critical swelling parameter is related to the critical channel radius and is calculated

as:

$$\eta_c = \phi \left(\frac{R_c}{R_o} \right)^{(1+\alpha)} \tag{3.12}$$

$$R_c = -\frac{2\gamma V_w \cos\theta}{R_g T \ln(RH)} \tag{3.13}$$

In this context, the symbol R_c denotes the critical channel radius, which is dependent on the variables T, RH, and θ. The R_c is employed in equation 3.12 for the computation of the η_c. η_c in equation 3.9 and P^l in equation 3.8 determines the ionomer network elements that will undergo swelling, resulting in the formation of a water channel within it. θ represents the contact angle of water on ionomer, V_w represents the molar volume of water, and RH represents the relative humidity to which the ionomer element is exposed. At a specific operating state, all variables become constant with the exception of η_{ij} and $\sigma_{o,ij}$. Thus, distinct swelling parameters are obtained for varied surface charge densities from equation 3.8. The channel radius within an ionomer element may be calculated using the swelling parameter. We'll call it equilibrium swollen channel radius R_{ij} and it's obtained as:

$$R_{ij} = R_o \left(\frac{\eta_{ij}}{\phi} \right)^{1/1+\alpha} \tag{3.14}$$

In electrochemical terms, λ represents the quantity of water molecules per sulphonic acid group and is used to quantify the ionomer's water uptake. Calculating the water uptake per element in the ionomer network will utilize the same definition. The

volume of water occupied in an ionomer element channel is calculated as:

$$V_c = \pi R_{ij}^2 l_I \tag{3.15}$$

Dividing this volume by the molar volume of water, V_w will provide us with the number of water molecules uptaken by an ionomer element. The total number of sulphonic acid group for an ionomer element channel is calculated as [16]:

$$N_{SO_3}^- = \frac{2\pi R_{ij} l_I \sigma(R_{ij})}{F} \tag{3.16}$$

Here, the surface charge density varies with radius as:

$$\sigma(R_{ij}) = \sigma_{o,ij} \left(\frac{R_o}{R_{ij}} \right)^{\alpha} \tag{3.17}$$

Thus, the water uptake by an element λ_{ij} becomes:

$$\lambda_{ij} = \frac{R_{ij} F}{\sigma(R_{ij}) V_w} \tag{3.18}$$

Hence, the total water uptake λ by the ionomer network for a given T and RH condition can be calculated by averaging the water uptake by each ionomer element. The volumetric change due to water uptake is calculated as described in [17]:

$$\frac{\Delta V}{V_o} = \text{IEC}\, \rho_p V_w \lambda \tag{3.19}$$

Table 3.1
Model parameters values

Properties	Value	Units	Source
Thermal conductivity, k^s	1.7	$\mathrm{Wm^{-1}K^{-1}}$	[9]
Phase change enthalpy Δh^e	2300 at 80^oC	$\mathrm{kJkg^{-1}}$	[9]
Solid heat capacity, $(\rho c_p)^s$	1.309×10^6	$\mathrm{Jm^{-1}K^{-1}}$	[9]
Liquid heat capacity, $(\rho c_p)^l$	4.134×10^3	$\mathrm{Jm^{-1}K^{-1}}$	[9]
Absolute permittivity, ϵ_o	8.854×10^{-12}	$\mathrm{Fm^{-1}}$	
Relative permittivity (30°C), ϵ_r	25		[15]
Universal gas constant, R_g	8.314	$\mathrm{JK^{-1}mol^{-1}}$	
Reference channel radius, R_o	1	nm	[16]
Faraday constant, F	96485	$\mathrm{C\,mol^{-1}}$	
Shear modulus (30°C), G	0.16	GPa	[15]
Gas pressure, P^g	101325	Pa	
Surface tension of water (30°C), γ	0.072	$\mathrm{Nm^{-1}}$	
Reorganization factor, α	0.5		
Density of dry polymer, ρ_p	2000	$\mathrm{kgm^{-1}}$	[15]
Ion exchange capacity, IEC	0.9	$\mathrm{mol\,kg^{-1}}$	[15]
Contact angle, θ	75°		
Molar volume of water, V_w	18×10^{-7}	$\mathrm{m^3mol^{-1}}$	
Boltzmann constant, k_B	1.38×10^{-23}	$\mathrm{J\ K^{-1}}$	

As we consider the overall volume of the catalyst layer and the carbon in the catalyst layer to be constant, any change in the volume of the ionomer network will have an immediate effect on the pore network. The total volume of the ionomer network will vary depending on the relative humidity, as individual ionomer elements will take in water and swell to their equilibrium radius and modify the void volume and, by extension, the porosity through volume conservation. We acquire all the constants necessary to explain this phenomenon from [16, 15], and [17], which are provided in Table 3.1.

Transport of protons through the ionomer network element is governed by electroosmotic drag, as defined by [18], excluding the diffusion term. The proton transport

thus becomes:

$$I_{ij} = \frac{4\pi q_e^2 c_o^2 g(\xi_{ij}) R_{ij}^4}{\mu l_I} dE_{ij} - \frac{\pi q c_o h(\xi_{ij}) R_{ij}^4}{2\mu l_I} dP_{ij} \tag{3.20}$$

I_{ij} is the proton current through an ionomer element, $q = -1.6 \times 10^{-19}$ is the electron charge. c_o is the proton concentration at the center of the ionomer element channel, and μ is the viscosity of water which is 3.5×10^{-4}Pa-s. dE_{ij} and dP_{ij} are the voltage and pressure gradient across the element. $g(\xi_{ij})$ is a function of dimensionless parameter ξ_{ij}, which is calculated as:

$$g(\xi_{ij}) = \frac{1}{2\xi_{ij}(1 - \xi_{ij}/8)} + \frac{4}{\xi_{ij}^2}\left(1 - \frac{\xi_{ij}}{8}\right) \tag{3.21}$$

The dimensionless parameter ξ_{ij} for an element is described as:

$$\xi = \frac{R_{ij} q^2 c_o}{\varepsilon \varepsilon_o k_B T} \tag{3.22}$$

The proton concentration at the channel center of an ionomer element, c_o is presented as:

$$c_o = \frac{8\sigma_{o,ij}}{\frac{q^2 R_{ij}^2 \sigma_o}{\varepsilon \varepsilon_o k_B T} - 4qR_{ij}} \tag{3.23}$$

$\sigma_{o,ij}$ is the surface charge density applied to the ionomer element, which is obtained from surface charge density distribution. k_B is the Boltzmann constant. Water is drawn along with the protons as they travel through an ionomer element. Water

movement is explained as:

$$\dot{M}_{ij} = \frac{4\pi\rho q c_o f(\xi_{ij}) R_{ij}^4}{\mu l_I} dE_{ij} - \frac{\pi\rho R_{ij}^4}{8\mu l_I} dP_{ij} \tag{3.24}$$

Here, $f(\xi)$ is a function of ξ which is expressed as:

$$f(\xi_{ij}) = \frac{1}{\xi_{ij}} \left[\frac{4}{\xi_{ij}} \ln \left(1 - \frac{\xi_{ij}}{8} \right)^{-1} - \frac{1}{2} \right] \tag{3.25}$$

The diffusion of water in the ionomer network element is modeled using Fick's law of diffusion. The liquid water flux is presented as:

$$q_{w,i} = \frac{D_w \pi R_{ij}^2}{l} (C_i - C_j) \tag{3.26}$$

$q_{w,i}$ is the total water generated due to oxygen reduction reaction in the catalyst particles around ionomer node i. C_i and C_j are the water vapor concentration at ionomer network nodes. D_w, the diffusivity of water in ionomer is a function of local λ and temperature T. It is calculated as in [19] as:

$$D_w = 2.5 \times 10^{-7} \lambda e^{(-2436/T)} \tag{3.27}$$

λ denotes water uptake by the ionomer network and it'll be the deciding factor for flooding initiation. Water activity in vapor phase a_v is obtained through water vapor

concentrations at the nodes. Then the water activity is used as [20] to obtain λ at the ionomer network nodes:

$$\lambda = 0.043 + 17.83a_v - 39.85a_v^2 + 36a_v^3 \tag{3.28}$$

Table 3.2
Distributed transport resistances throughout the networks

Network	Transport resistances	Value	Unit
Pore	Liquid water permeability	$\kappa \frac{r_{ij}^4}{\mu_{ij}^{\text{eff}} l}$	$\text{m}^3\text{Pa}^{-1}\text{s}^{-1}$
Pore	Gas diffusion resistance	$\frac{\pi r_{ij}^2 D^{g,a}}{l}$	m^3s^{-1}
Carbon	Heat conductance resistance	$\frac{k^s \pi (rs)_{ij}^2}{l}$	WK^{-1}
Ionomer	Water diffusion resistance	$\frac{D_w \pi R_{ij}^2}{l}$	m^3s^{-1}
Ionomer	Electric conductance resistance	$\frac{4\pi q_e^2 c_o^2 g(\xi_{ij}) R_{ij}^4}{\mu l_I}$	$\text{CV}^{-1}\text{s}^{-1}$
Ionomer	Permeation resistance of proton	$\frac{\pi q c_o h(\xi_{ij}) R_{ij}^4}{2\mu l_I}$	$\text{CV}^{-1}\text{s}^{-1}$

3.1.6 Oxygen reduction reaction

Using a double trap kinetic model enables the acquisition of the electrochemical current produced by an aggregate of carbon, catalysts, pores, and ionomers which is well documented by Zenyuk [21, 22]. The study by Liu [13] involved modifications to the double trap kinetic model in determining the quantity of current produced by individual catalyst particles. This methodology has been incorporated into our model.

Chapter 4

Coupling Algorithm

4.1 Coupling the Networks

From the GDL side, oxygen diffuses into the catalyst layer and fills its pores. Electroosmotic drag transports protons along the ionomer network's elements. The O_2 concentrations at the platinum surface and the generated current is calculated as in [13]. Water is retained by the ionomer, which increases the local water concentration through equation 3.27 and water uptake within the ionomer network as specified in equation 3.28. It has been found by Kusoglu and Shrivastava [23, 24] that the water retention capacity of the thin ionomer film of the catalyst layer is lower than that of the ionomer in the proton exchange membrane. Therefore, the maximum λ for

ionomer network elements is 5, which is based on an average of λ values found in the literature. If λ is more than 5, the extra water injected into the adjacent pore network elements. Finding the path of least resistance, water forms menisci and percolates through the pore network as discussed in equation 3.4. The simulation algorithm and coupling method are summarized in Figure 4.1.

4.1.1 Water diffusion in ionomer

Water instantly diffuses into the ionomer network components around catalyst particles from the oxygen reduction event. As we can see from Figure 4.2, liquid water floods the catalyst layer pore network and the λ in the same region of the ionomer network is restricted to a value less than 5.

4.1.2 Prediction of local water distribution

Liquid water follows the route of least resistance in the pore network, passing from one pore element to the next. Because the orientation of the pore elements varies from realization to realization, the saturation profile and the percolation time also change which can be observed in the Figures 4.4 and 4.5 respectively. For realization 1 in Figure 4.4, the invasion started in 2s and the liquid menisci reached the GDL

within 14s. While the percolation in realization 2 in figure 4.5 started at 4s and even after 20s the invasion didn't stop as evaporation is preventing liquid water menisci from the GDL boundary. Water is removed in the vapor phase in this case.

In the current network model, excess water is injected into the elements located at along the PEM boundary. One of the proposed activities is to enable liquid water injection at the pore elements adjacent to the catalyst sites.

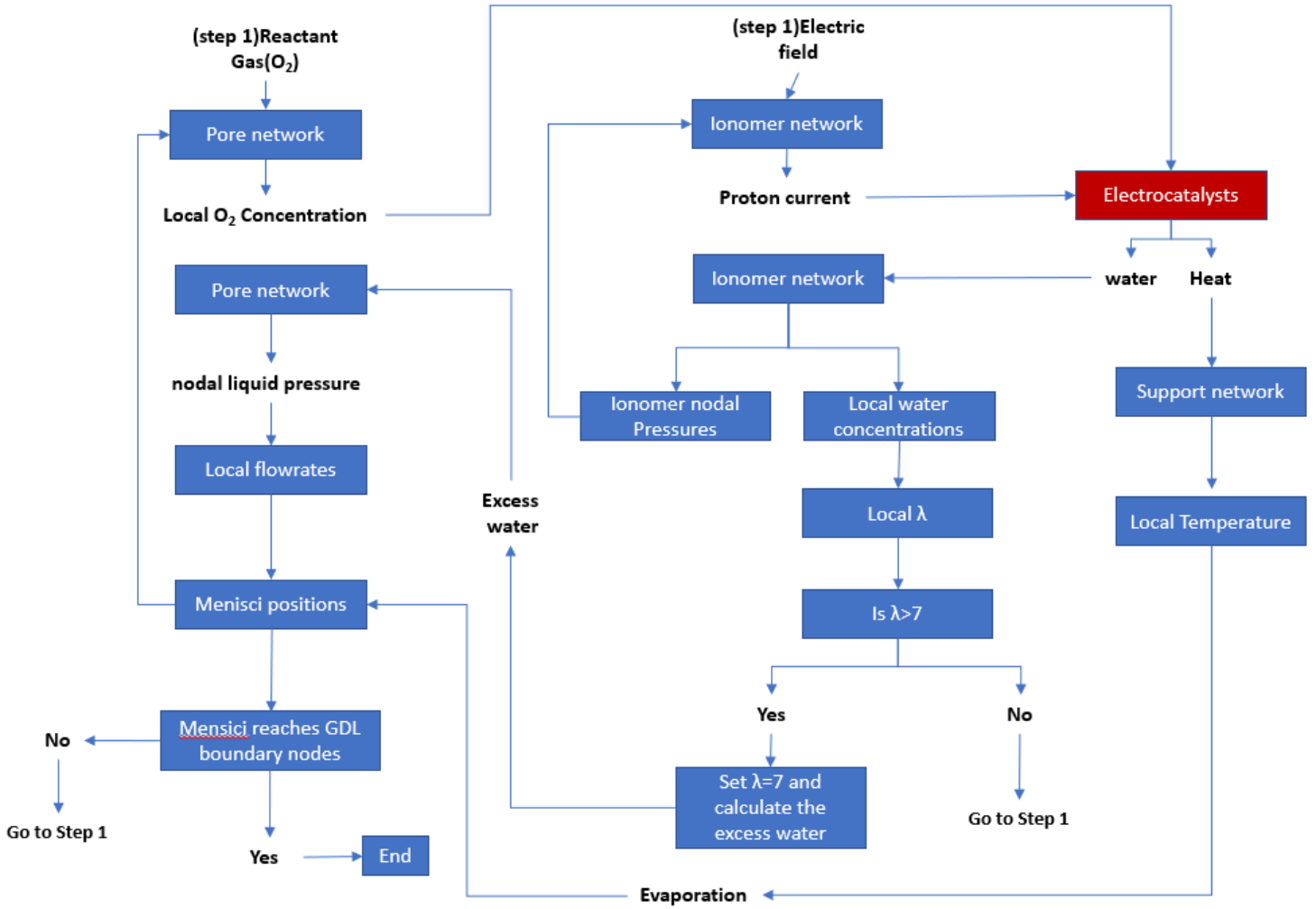

Figure 4.1: Flow chart for the coupling process and simulation algorithm

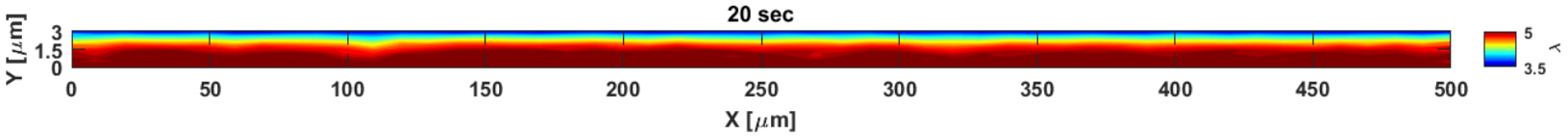

Figure 4.2: λ distribution in the ionomer network of the catalyst layer realization 1 at 40^oC and $90\%RH$. South boundary is PEM and north boundary is GDL

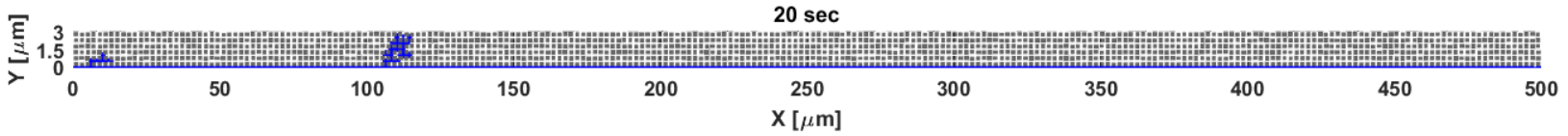

Figure 4.3: Local water balance in pore space of realization 1 at 40^oC and $90\%RH$. South boundary is PEM and north boundary is GDL

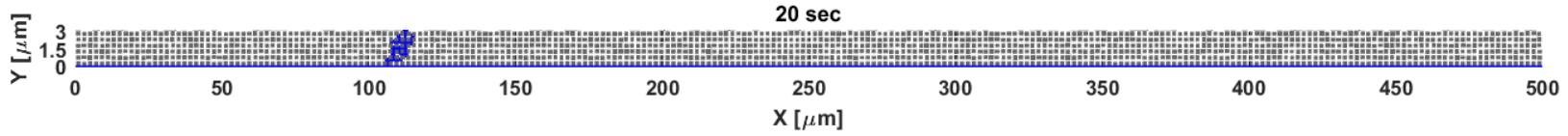

Figure 4.4: Local water saturation profile for catalyst layer pore-space realizations 1. Operating conditions are 80^oC and $90\%RH$. The south boundary is PEM and north boundary is GDL

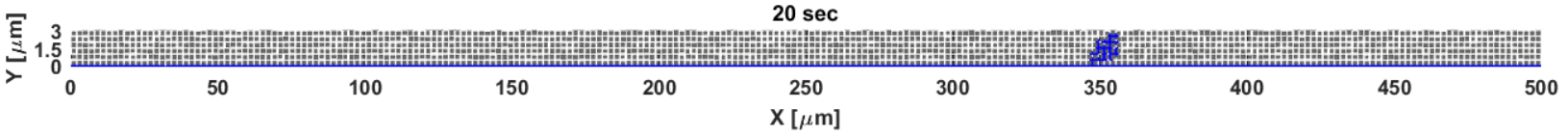

Figure 4.5: Local water saturation profile for catalyst layer pore-space realizations 2. Operating conditions are 80^oC and $90\%RH$. The south boundary is PEM and north boundary is GDL

4.1.3 Local O_2 distribution

Water diffusion of O_2 was insignificant as discussed in gas diffusion in pore network. Hence, local flooding lowers O_2 concentration in the pore network, denying reactant gas to the active sites for oxygen reduction. O_2 concentration profile varies with the local water saturation profile from one realization to another although the average O_2 concentration remains the same. Here, only the concentration profile of O_2 for

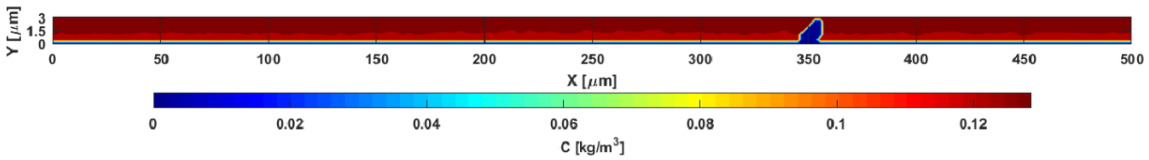

Figure 4.6: Local O_2 distribution in the pore space of catalyst layer realization 2 at 80^oC and $90\%RH$. South boundary is PEM and north boundary is GDL

realization 1 is shown in Figure 4.6.

4.1.4 Active site distribution

During the current generation, water is produced as a byproduct of the oxygen reduction reaction at the active sites. As the ionomer capacity for retaining water is exceeded, water enters the pore space, leaving some of the active regions depleted of O_2. When the amount of water invading the pore network increases, more pore ele-

ments are flooded, leading to fewer active regions in the catalyst layer and, thus, less current being produced. Figure 4.7 and 4.8 demonstrate the distribution of active sites for flooding regions at the beginning and end of the simulation respectively.

4.1.5 Temperature profile

The catalyst layer has a uniform constant temperature of 80^oC at the start of the simulation. As soon as the simulation begins, the active regions' temperature increases due to electrochemical reactions. Once flooding begins, the number of active sites decreases, and the temperature in that region drops (at around 340μm to 360μm region) which is observed by comparing initial and final temperature distribution in Figure 4.9 and 4.10. fraction of the heat generated is absorbed by evaporating liquid water mass.

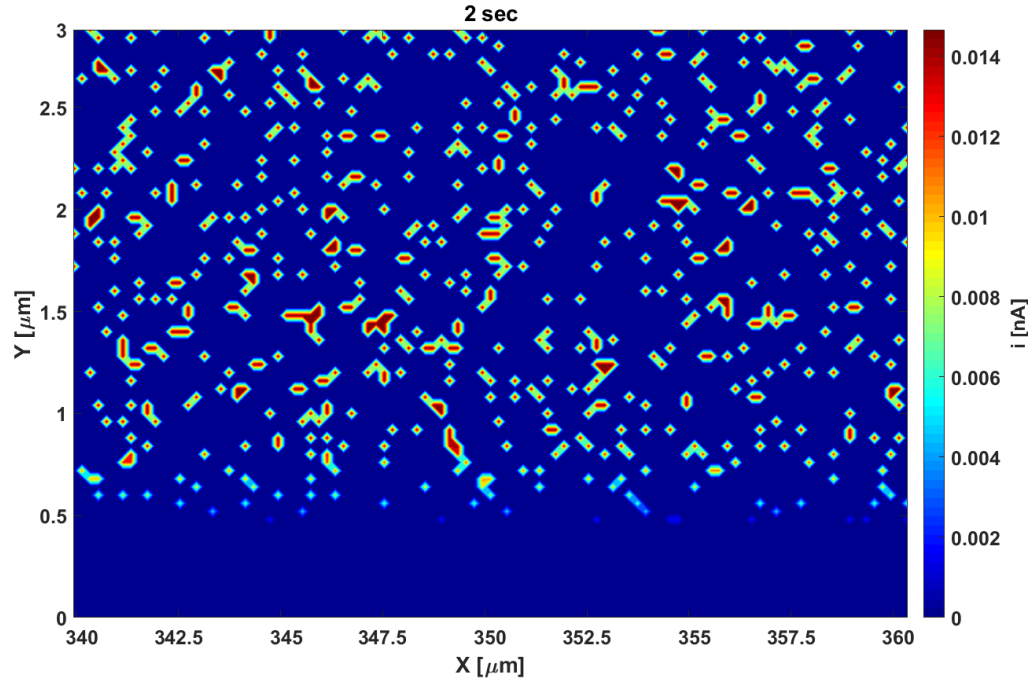

Figure 4.7: active site distribution for realization 2 at the beginning of the simulation at 80^oC and $90\%RH$. The south boundary is PEM and the north boundary is GDL

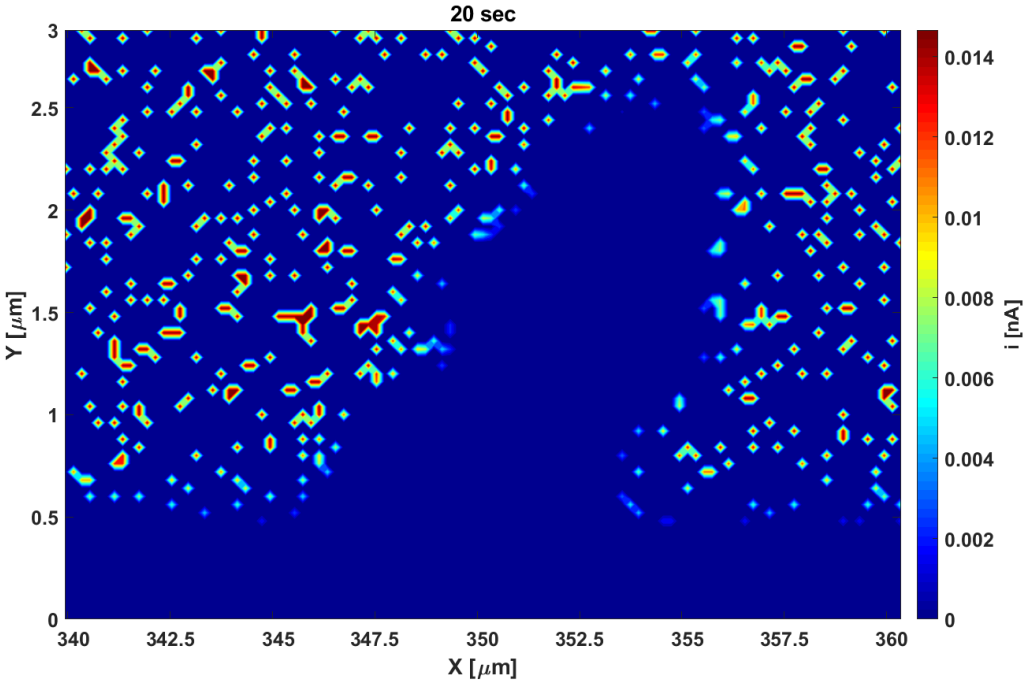

Figure 4.8: active site distribution for realization 2 at the end of the simulation at 80^oC and $90\%RH$. The south boundary is PEM and the north boundary is GDL

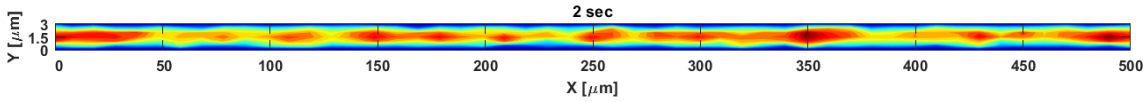

Figure 4.9: initial temperature distribution in the carbon network for realization 2. The south boundary is PEM and the north boundary is GDL

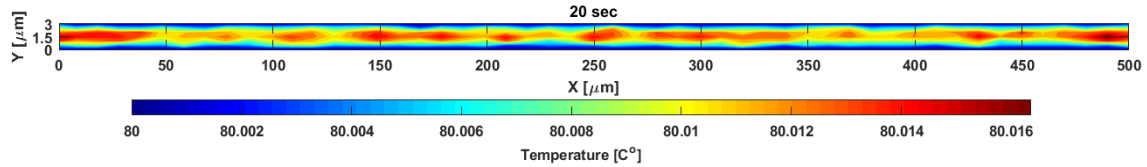

Figure 4.10: Temperature distribution after breakthrough in the carbon network for realization 2. The south boundary is PEM and the north boundary is GDL

Chapter 5

Project Tasks Going Forward

5.1 Model development

5.1.1 Ionomer surface charge distribution

The properties of the ionomer material, environmental operating conditions, and surface charge density distribution all play a role in the swelling of the ionomer network. A distribution of surface charge density will be generated to create an ionomer network, and the surface charges will be randomly applied to the ionomer network elements. Ionomer network elements with differing surface charges would obtain various swollen channels, as described in 3.1.5, and this is how we'll introduce

local heterogeneity in the ionomer of the catalyst layer.

5.1.2 Ionomer water uptake submodel

After the water is generated, the concentration of the ionomer increases, leading to the rise in the λ (as explained in 4.1.1). However, the ionomer water uptake is relatively slow [23]. To capture the appropriate physics of water uptake by the catalyst layer ionomer, we will introduce the time constants in the water uptake mechanism from [23] and combine it with the equations in 3.1.5.

5.1.3 Porosity and Pore size distribution shift with RH

The volume of the catalyst layer and the volume contained by the carbon network of the catalyst layer is held constant. So, the volume expansion by the ionomer at various relative humidity will cause only the pore volume, i.e., the porosity, to reduce. As a result, each RH condition will produce a new porosity, and the porosity will create a new pore size distribution for the pore-phase network.

5.1.4 Localized water injection

Local flooding will occur due to condensation, which is initiated when any pore network node becomes saturated with water vapor or relative humidity exceeds 100%. This is a novel feature of our present modeling strategy, which is similar to capturing condensation in GDL using pore-network by Straubhaar [25] and Hinebaugh [26]. We expect the local water pattern to be comparable to those depicted in Figures 4.4 and 4.5. However, when liquid water starts flooding the void space, the menisci that reach the breakthrough may vary.

5.1.5 H^+ transport due to pressure gradients

As a result of local flooding, liquid water will exert pressures at the ionomer nodes. Large pressure gradients are anticipated, which restrict proton transport in the ionomer network. We will investigate the conditions under which proton limited transport can occur due to adverse pressure differences.

5.2 Model validation

5.2.1 Pore network

Fluid will be injected into the pore network at different flow rates. The percolation behavior of the fluid in the generated network will be compared against experimental data to validate the macro and microscopic properties of the pore network

5.2.2 Ionomer network

The water uptake data and volumetric expansion of the thin ionomer film of the catalyst layers will be compared to the water uptake and swelling behavior of the generated ionomer network to confirm the validity of the ionomer network's surface charge density distribution.

5.2.3 Polarization predictions

The model will provide current densities for various cell voltages. Voltages and current densities will generate polarization curves at different temperatures and relative

humidities, which will be compared to those produced by experiments to validate the coupling algorithm.

5.3 Parametric studies

5.3.1 Proton limited transport study

Due to a large amount of water generation and liquid pressure gradients, active sites are predicted to become proton-starved after a certain simulation time as a consequence of local flooding.

5.3.2 Graded ionomer distribution study

The distribution of ionomer surface charge density can have a substantial impact on the proton conduction and water management of catalyst layers, which will be investigated in this parametric study.

5.3.3 Project Timeline & Milestones

Table 5.1
Project timeline and milestones (Quartile 3 of year 1 starts from July 2023)

Task	*Year 1*		*Year 2*				*Year 3*	
	Q3	Q4	Q1	Q2	Q3	Q4	Q1	Q2
8.1 Model Development								
8.1.1 Ionomer surface charge distribution	▬							
8.1.2 Ionomer water uptake submodel		▬						
8.1.3 Porosity and PSD change with RH		▬						
8.1.4 Localized water injection				▬				
8.1.5 H^+ transport due to ΔP					▬	▽		
8.2 Model Validation								
8.2.1 Pore network validation		▬	▬					
8.2.2 Ionomer network validation		▬						
8.2.3 Polarization curve predictions						▬▽		
8.3 Parametric Studies								
8.3.1 Graded ionomer distribution study							▬▽	
8.3.2 Proton-limited transport study								▬▽

References

[1] Ioannidis, M. A.; Chatzis, I. *Chemical Engineering Science* **1993**, *48*(5), 951–972.

[2] Chang, D.; Ioannidis, M. *Journal of colloid and interface science* **2002**, *253*(1), 159–170.

[3] Aker, E.; Måløy, K. J.; Hansen, A.; Batrouni, G. G. *Transp. Porous Media* **1998**, *32*(2), 163–186.

[4] Al-Gharbi, M. S.; Blunt, M. J. *Physical Review E* **2005**, *71*(1), 016308.

[5] Raoof, A.; Nick, H. M.; Hassanizadeh, S. M.; Spiers, C. *Computers & Geosciences* **2013**, *61*, 160–174.

[6] Gostick, J. T.; Ioannidis, M. A.; Fowler, M. W.; Pritzker, M. D. *J. Power Sources* **2007**, *173*(1), 277–290.

[7] Sinha, P. K.; Wang, C.-Y. *Electrochimica Acta* **2007**, *52*(28), 7936–7945.

[8] Medici, E.; Allen, J. *Journal of The Electrochemical Society* **2010**, *157*(10), B1505.

[9] Médici, E. F.; Allen, J. S. *Int. J. Heat Mass Transf.* **2013**, *65*, 779–788.

[10] El Hannach, M.; Prat, M.; Pauchet, J. *Int. J. Hydrogen Energy* **2012**, *37*(24), 18996–19006.

[11] El Hannach, M.; Pauchet, J.; Prat, M. *Electrochim. Acta* **2011**, *56*(28), 10796–10808.

[12] Konduru, V.; Allen, J. S. *ECS Transactions* **2017**, *80*(8), 65.

[13] Liu, J.; Medici, E.; Haug, A. T.; Cullen, D. A.; Tajiri, K.; Allen, J. S.; Zenyuk, I. V. *International Journal of Hydrogen Energy* **2022**, *47*(40), 17749–17761.

[14] Nguyen, T. V.; White, R. E. aug **1993**, *140*(8), 2178.

[15] Eikerling, M. H.; Berg, P. *Soft matter* **2011**, *7*(13), 5976–5990.

[16] Berg, P.; Nadon, P. *Soft Matter* **2021**, *17*(24), 5907–5920.

[17] Safiollah, M.; Melchy, P.-E. A.; Berg, P.; Eikerling, M. *The Journal of Physical Chemistry B* **2015**, *119*(25), 8165–8175.

[18] Berg, P.; Findlay, J. *Proc. R. Soc. A Math. Phys. Eng. Sci.* **2011**, *467*(2135), 3157–3169.

[19] Fuller, T. F. *Solid-polymer-electrolyte fuel cells;* University of California, Berkeley, 1992.

[20] Springer, T. E. *Journal of The Electrochemical Society* **1991**, *138*(8), 2334.

[21] Zenyuk, I. V.; Das, P. K.; Weber, A. Z. *Journal of the Electrochemical Society* **2016**, *163*(7), F691.

[22] Moore, M.; Wardlaw, P.; Dobson, P.; Boisvert, J.; Putz, A.; Spiteri, R.; Secanell, M. *Journal of the Electrochemical Society* **2014**, *161*(8), E3125.

[23] Kusoglu, A.; Kwong, A.; Clark, K. T.; Gunterman, H. P.; Weber, A. Z. *Journal of The Electrochemical Society* **2012**, *159*(9), F530.

[24] Shrivastava, U. N.; Fritzsche, H.; Karan, K. *Macromolecules* **2018**, *51*(23), 9839–9849.

[25] Straubhaar, B.; Pauchet, J.; Prat, M. *International Journal of Heat and Mass Transfer* **2016**, *102*, 891–901.

[26] Hinebaugh, J.; Bazylak, A. *Journal of the Electrochemical Society* **2010**, *157*(10), B1382.